

1 **Title**

2 Visual function at the atrophic border in choroideremia assessed with adaptive optics
3 microperimetry

4
5 **Authors**

6 William S. Tuten^{1,2,*}; Grace K. Vergilio^{1,3}; Gloria J. Young^{1,3}; Jean Bennett^{1,3}; Albert M.
7 Maguire^{1,3}; Tomas S. Aleman^{1,3}; David H. Brainard²; Jessica I.W. Morgan^{1,3}

8
9 ¹Scheie Eye Institute, Ophthalmology, University of Pennsylvania, Philadelphia, PA, United
10 States

11 ²Department of Psychology, University of Pennsylvania, Philadelphia, PA, United States

12 ³Center for Advanced Retinal Ocular Therapeutics, University of Pennsylvania, Philadelphia,
13 PA, United States

14 *Current address: School of Optometry, University of California, Berkeley, Berkeley, CA, United
15 States

16
17 **Meeting presentation:**

18 Results from this study were presented in part at the Association for Research in Vision and
19 Ophthalmology 2018 annual meeting.

20
21 **Financial Support:**

22 This manuscript was supported by NIH R01EY028601, NIH U01EY025477, NIH P30
23 EY001583, Research to Prevent Blindness Stein Innovation Award, Foundation Fighting
24 Blindness, the F. M. Kirby Foundation, the Paul and Evanina Mackall Foundation Trust,
25 Pennsylvania Lions Sight Conservation, Eye Research Foundation, Brenda and Matthew
26 Shapiro Stewardship, and the Robert and Susan Heidenberg Investigative Research Fund for
27 Ocular Gene Therapy. The content is solely the responsibility of the author and does not
28 necessarily represent the official views of the National Institutes of Health.

29
30 **Acknowledgements:**

31 The authors thank Robert F. Cooper for technical assistance, Alfredo Dubra for sharing the
32 AOSLO optical design, as well as AO control, image acquisition and image registration
33 software, and Austin Roorda for sharing the AO microperimetry design and software.

34

35 **Conflict of Interest:**

36 JIWM is an inventor on US Patent 8,226,236 and receives funding from AGTC. WST is an
37 inventor on US Patent 10,130,253. JIWM, WST, and DHB have filed a provisional patent. JB
38 and AMM have a patent licensed by Spark Therapeutics, but waived potential financial gain. JB
39 serves as an advisor for Gensight Biologics, Perch Therapeutics and Akouos, and receives
40 funding from Biogen and Limelight. AMM receives funding from Spark Therapeutics. All other
41 authors report no conflict of interest.

42

43 **Running head:**

44 Visual function at the atrophic border in choroideremia

45

46 **Address for reprints:**

47 Attention: Jessica I. W. Morgan

48 3400 Civic Center Blvd.

49 Ophthalmology, 3rd floor West, 3-112W

50 Philadelphia, PA 19104

51 jwmorgan@pennterapeutics.com

52

53 **Précis:** Adaptive optics microperimetry revealed sharp functional transitions that co-located
54 between relatively intact and severely-degenerated retina in choroideremia. Outer retinal
55 tubulations containing cone inner segments did not exhibit measurable visual sensitivity when
56 probed with cellular-scale stimuli.

57 **Abbreviations:**

58 ADD: Airy disk diameters

59 AO: adaptive optics

60 AOM: acousto-optic modulator

61 AOSLO: adaptive optics scanning laser ophthalmoscopy

62 CHM: Choroideremia

63 dB: decibels

64 ELM: external limiting membrane

65 FAF: fundus autofluorescence

66 OCT: optical coherence tomography

67 ORT: outer retinal tubulation

- 68 PMT: photo-multiplier tube
- 69 REP1: rab escort protein 1
- 70 RPE: retinal pigment epithelium
- 71 TCA: transverse chromatic aberration

72 **Abstract**

73 Purpose: Recent advances in retinal imaging allow visualization of structural abnormalities in
74 retinal disease at the cellular level. Here we use adaptive optics (AO) microperimetry to assess
75 visual sensitivity with high spatial precision and examine how function varies across two
76 phenotypic features observed in choroideremia (CHM) – atrophic lesion borders and outer
77 retinal tubulations (ORTs).

78 Design: Cross-sectional study.

79 Subjects: 12 CHM patients.

80 Methods: A custom adaptive optics scanning light ophthalmoscope (AOSLO) equipped with
81 both confocal and non-confocal split-detection imaging modalities was used to image the
82 photoreceptor inner and outer segment mosaics. For AO microperimetry, circular 550-nm stimuli
83 were presented through the AOSLO system; stimuli were either 9.6 or 38.3 arcmin² (~60 or 15
84 times smaller than a Goldman III stimulus). Test locations were identified in structural images
85 and stimuli were targeted to these locations using real-time retinal tracking combined with
86 measurements of transverse chromatic aberration. Psychophysical detection thresholds were
87 measured at the atrophic border in 12 patients. Additionally, visual sensitivity was probed along
88 ORTs in four patients.

89 Main Outcome Measure: Visual sensitivity thresholds measured with AO microperimetry at
90 retinal locations corresponding to structural phenotypes observed in AOSLO retinal images.

91 Results: In CHM, sharp borders between intact central islands of the photoreceptor mosaic and
92 complete atrophy of the outer retina and retinal pigment epithelium were observed in both split
93 detection and confocal structural images. AO microperimetry at locations spanning these
94 borders show a commensurately sharp decrease in function, with readily measurable visual
95 sensitivity on one side and dense scotoma on the other. These functional transitions often
96 occurred over a distance smaller than the diameter of the Goldman III stimulus. Thresholds
97 measured along ORTs showed dense scotoma over the tubule in all four subjects, despite the
98 visibility of remnant cone inner segments in the AO images.

99 Conclusions: CHM patients exhibit sharp functional transitions that collocate with structural
100 transitions from intact to severely degenerated retina. We found no evidence of visual sensitivity
101 over ORTs. Measuring cone function with high resolution offers insight to disease mechanisms
102 and may enable precise assessment of whether experimental therapies, such as gene therapy,
103 provide a functional benefit.

104

105

106 **Introduction**

107 Choroideremia (CHM) is an X-linked inherited retinal degeneration with a prevalence of
108 approximately 1 in 50,000.¹ CHM is caused by mutations in the *CHM* gene, which interrupt the
109 encoding of rab-escort protein 1 (REP1).² REP1 is involved in the prenylation of Rab proteins
110 which are necessary for intercellular trafficking and phagocytosis.³ Lack of functional REP1
111 results in progressive degeneration of the photoreceptors, retinal pigment epithelium (RPE), and
112 choroid.^{4, 5} In CHM patients, with established disease and central retinal involvement, fundus
113 appearance is characterized by a central island of relatively preserved retina and RPE with
114 characteristic scalloped edges, surrounded by atrophic, depigmented retina (Figure 1A).⁵
115 Structurally, a sharp transition between atrophic and relatively preserved, ostensibly viable,
116 retina is suggested by retained central fundus autofluorescence (FAF) (Figure 1B).⁶ Optical
117 coherence tomography (OCT) has shown initial layer disruption occurring in the interdigitation
118 zone between the photoreceptor tips and the RPE,⁶ and inner retinal thickening within the
119 central island.⁴ Interlaminar bridges mark the transition from the central island to atrophic areas
120 showing loss of outer retinal layers and loss of RPE pigmentation.⁷ OCT imaging has also
121 shown that a high proportion of CHM patients exhibit outer retinal tubulations (ORTs) peripheral
122 to the central island (Figure 1C, arrowheads).^{4, 8}

123 At a broad level, loss of visual function in CHM progresses essentially in lockstep with the
124 pattern of structural degeneration.^{4, 8} Initial symptoms include nyctalopia and peripheral visual
125 field loss.⁵ Progressive functional loss proceeds centripetally and centrifugally from the
126 midperiphery degeneration leading to tunnel vision and ultimately blindness. High visual acuity
127 is commonly maintained and only becomes compromised in later stages of the disease, as
128 degeneration encroaches on the central fovea.^{4, 9} Cone and rod sensitivity losses in CHM are
129 detectable within the midperipheral and/or central retina from the earliest disease stages.⁴
130 Clinical microperimetry shows that CHM patients have an absolute scotoma in the atrophic area
131 corresponding to loss of the outer retina and RPE, but can have either normal or reduced
132 sensitivities within the centrally retained retinal area.^{10, 11}

133 Currently there are no approved treatments for CHM, although multiple gene therapies are
134 currently being tested in clinical trials with some indications of success.^{12, 13} Gene therapeutic
135 approaches aim to restore function to surviving cells. Thus, there is a critical need to understand
136 both the extent to which cellular structure remains intact in CHM and how cellular structure
137 correlates with visual function. Studies addressing these issues are critical for guiding the
138 targeting and assessment of gene therapies (as well as other therapeutic approaches), and for
139 maximizing the sensitivity of outcome measures for assessing therapeutic safety and efficacy.

140 Adaptive optics (AO) ophthalmoscopy has enabled the acquisition of retinal images with
141 cellular resolution.¹⁴ AO studies in CHM have shown that the cone photoreceptor mosaic
142 remains present and contiguous up to the atrophic border between the central island of
143 preserved retina and the peripheral atrophy.^{6, 15, 16} Using adaptive optics scanning laser
144 ophthalmoscopy (AOSLO), our group previously showed that some local regions within the
145 retained central island exhibit normal cone density while others showed reduced cone density.⁶
146 While these studies provide important descriptions of the cellular structural phenotype of CHM,
147 they have not related retained cellular structure to visual function at the same high spatial
148 resolution.

149 Here, we measure both retinal structure and visual function in CHM with high spatial
150 resolution. We combine AO with microperimetry to examine CHM patients' visual sensitivity to
151 very small stimuli targeted to retinal locations just inside the atrophic border (regions showing
152 preserved photoreceptor structure) in comparison to retinal locations just outside the atrophic
153 border (regions showing loss of the photoreceptor mosaic). Our results show a sharp transition
154 in retinal function that closely follows the co-localized changes in photoreceptor structure. We
155 further targeted small visual stimuli along ORTs and at retinal locations adjacent to ORTs but
156 just inside the atrophic border. Our results again show a sharp transition in retinal function, with
157 loss of sensitivity at retinal locations corresponding to ORTs.

158 Our results provide a better understanding of disease mechanisms at play in CHM, and
159 have implications for applying both structural and functional outcome measures to assess CHM
160 disease progression and treatment efficacy.

161

162 **Methods**

163 Subjects

164 12 male subjects with CHM (Table 1) participated in this study. Eight of these were part of
165 an ongoing longitudinal study evaluating the efficacy of a gene therapy intervention. All data
166 presented in this study from patients in the intervention group were collected from the untreated
167 eye but were collected after the gene therapy had been delivered to the contralateral eye. This
168 study was approved by the Institutional Review Board the University of Pennsylvania. All study
169 procedures adhered to the principles enumerated in the Declaration of Helsinki. Prior to
170 enrollment, the nature of the study and its associated risks were explained, and informed
171 consent was obtained from each subject.

172

173 Clinical Measurements of Retinal Structure and Function

174 Subjects underwent a comprehensive ophthalmic exam, including axial length
175 measurement, fundus photography, spectral domain OCT cross-sectional imaging, short
176 wavelength FAF imaging (Spectralis, Heidelberg Engineering, Carlsbad, CA), visual sensitivities
177 with a commercially available instrument (Nidek, MP-1, Fremont, CA) using a conventional 10-2
178 protocol grid and an achromatic Goldman size III stimuli presented to the dark-adapted eye (30
179 min adaptation period) on a 1.27 cd/m² background. Some subjects were able to return at a
180 different date for additional testing, at which point, all procedures were repeated. Molecular
181 testing by a CLIA laboratory was carried out to confirm the diagnosis of CHM. Subject
182 information can be found in **Table 1**.

183

184 Imaging the Retina with Adaptive Optics Scanning Light Ophthalmoscopy

185 Prior to AOSLO imaging, subjects' pupils were dilated using 1% tropicamide and 2.5%
186 phenylephrine ophthalmic solutions. Once mydriasis was achieved, subjects were aligned to the
187 AOSLO imaging beam using a bite bar fitted with a custom dental impression. Subject fixation
188 was guided by a secondary light source viewed through a pellicle beam splitter.

189 The details of imaging the retina with a multimodal AOSLO have been described
190 elsewhere.^{17, 18} The AOSLO system used in this study featured three input wavelengths: 848 nm
191 (for wavefront sensing), 795 nm (for retinal imaging), and 550 nm (for visual stimulation; see
192 below). To ensure each input channel would be well focused on the retina, the relative
193 vergences of the three beams were adjusted to compensate for longitudinal chromatic
194 aberration of the human eye according to normative data.¹⁹ The input beams were co-aligned
195 prior to entry into the main optical path, where they were scanned across the retina in a raster
196 pattern by vertical and horizontal scanning mirrors positioned in optical planes conjugate to the
197 pupil. The light returning from the eye was descanned and entered the collection arm of the
198 system. For 795 nm light, three photo-multiplier tubes (PMTs) were arrayed to detect incoming
199 photons. One PMT was positioned behind a pinhole (1.13 Airy Disk Diameters [ADD]) to provide
200 a confocal image of the cone mosaic, whereas the remaining PMTs were arranged in a non-
201 confocal split-detector configuration to sense multiply-scattered light.¹⁸ The 550 nm collection
202 channel also featured a confocal PMT (1.40 ADD pinhole) for concurrent imaging at the stimulus
203 wavelength. The 848nm light was directed towards a Shack-Hartmann wavefront sensor to
204 monitor ocular aberrations, which were corrected in closed-loop using a 97-actuator deformable
205 mirror (DM97-15, ALPAO, Montbonnot-Saint-Martin, France).

206 The angular size of the imaging raster was determined by analyzing images of a Ronchi
207 ruling acquired with either a horizontal or vertical orientation; the former was also used to

208 measure and correct for the sinusoidal image distortion introduced by the horizontal resonant
209 scanner. Visual angle units may be converted to microns on the retina using axial length
210 measurements obtained with a Zeiss IOLMaster (Carl Zeiss Meditec, Jena, Germany) and
211 provided in Table 1, according to previously published methods.²⁰ For structural AO imaging, a
212 1-by-1 degree imaging raster was used; for AO microperimetry, the imaging field was expanded
213 to subtend roughly 1.5-by-1.5 degrees (see *Adaptive Optics Microperimetry* below).

214 To assess cone mosaic structure, spatially overlapping AOSLO videos were acquired at and
215 surrounding each retinal location tested with AO microperimetry. Each AOSLO video comprised
216 150 frames acquired at 16.7 Hz. Video frames were aggregated offline using custom strip-
217 registration software.²¹ The near-infrared detector configuration enabled the concurrent
218 acquisition of confocal (outer segments) and split-detector (inner segments) retinal images with
219 cellular resolution.¹⁸

220

221 Adaptive Optics Microperimetry

222 The AOSLO used to image the retina in this study was also equipped with microperimetry
223 capabilities—i.e., the ability to track the moving retina and deliver visual stimuli to targeted
224 loci.^{22, 23} To achieve tracking, retinal videos were digitized by a field-programmable gate array
225 (FPGA) board and relayed strip-by-strip to a graphics processing unit (GPU) for real-time
226 stabilization and retinal position estimation via strip-based registration to a reference image²⁴.
227 The stabilized videos were displayed in a custom video rendering interface, and retinal locations
228 targeted for perimetric testing were selected manually in stabilized image coordinates by the
229 examiner.²⁵ Stimuli were delivered pixel-by-pixel by modulating the intensity of the scanned
230 stimulus beam with an acousto-optic modulator (AOM; Brimrose Corp., Sparks, MD, USA). The
231 timing of stimulus delivery was guided by the GPU, which used retinal position information to
232 generate a prediction of when the scanned beam would encounter the retinal target and, thus,
233 when the AOM should be triggered by the FPGA board. Delivery predictions were generated
234 independently for each frame of stimulus delivery. Delivery locations were encoded directly into
235 each delivery frame by inserting a digital marker at the image pixel corresponding to the center
236 of the rendered stimulus.

237 For AO microperimetry, the imaging field size was set to 1.5-by-1.5 degrees. The rationale
238 behind this choice is that the image-based eye tracking algorithm requires some overlap
239 between the reference image and subsequent video frames to achieve a successful registration.
240 The image shift, in pixels, associated with a fixational eye movement of fixed magnitude will
241 increase as the imaging field size decreases (assuming the pixel sampling rate remains

242 constant). By contrast, imaging over larger fields can also hamper image-based retinal tracking
243 due to degradations in image quality associated with undersampling and the difficulty of
244 correcting high-order ocular aberrations across non-isoplanatic fields. The 1.5° imaging field
245 size used in this study thus represents a practical middle ground, providing sufficient resolution
246 for the image-based retinal tracking algorithm while still remaining tolerant of ordinary fixational
247 eye motion, ultimately producing fewer tracking failures and more successful stimulus deliveries.

248 Microperimetry stimuli were 550 ± 15 nm (chosen to equate the sensitivity of the long- and
249 middle-wavelength-sensitive cone photoreceptors) and circular in shape, with diameters of
250 either 3.5 or 7.0 arcmin. For comparison, the standard Goldmann III stimulus used routinely in
251 clinical microperimetry subtends approximately 26 arcmin (0.43°). Note also that because our
252 stimuli are delivered through the AO system, their retinal size is not increased because of
253 blurring by the eye's normal optical point spread function. Stimulus size was chosen by the
254 examiner based on the test eccentricity and a preliminary assessment of the local visual
255 sensitivity. Specifically, at the beginning of each session, one or two 20-trial practice runs were
256 conducted to familiarize the subject with the response paradigm (see below). For these trials,
257 retinal tracking was disabled to ensure the stimulus was delivered on every trial (albeit at slightly
258 different retinal locations from one trial to the next, depending on fixational eye movement).
259 Stimuli in the practice runs were centered away from the atrophic border so that most trials
260 landed in the contiguous cone mosaic. Stimulus size was deemed appropriate if the threshold
261 algorithm (see below) converged on a value near the lower-half of the dynamic range of the
262 system; this allowed enough headroom for higher thresholds to be measured as the lesion
263 border was approached. If the preliminary threshold estimate was near the upper end of the
264 system's dynamic range, we opted for the larger stimulus size to bring the thresholds down.
265 Note that for a given subject and eccentricity, stimulus size was kept constant for all test
266 locations.

267 For each test location, increment threshold was determined using a 20-trial adaptive
268 staircase²⁶ guided by a yes-no response paradigm and set to converge on the test intensity
269 producing a 78% frequency-of-seeing. Subject responses were recorded using a programmable
270 game controller. The subject initiated each trial by button press, which triggered the recording of
271 a one-second retinal video during which the stimulus was delivered for three frames (187.5 ms)
272 to the targeted location. Stimulus delivery was accompanied by an audible cue, and delivery
273 locations were encoded into the retinal videos via a digital marker corresponding to the center
274 pixel of the AOM-rendered stimulus. Subjects indicated whether the stimulus was “seen” or “not

275 seen” by pressing buttons corresponding to those responses on the game controller. A “repeat
276 trial” button was also available, although its use was reserved for instances where the examiner
277 observed failed deliveries during the experiment (e.g., due to blinks, tear film evaporation, drifts
278 in fixation, or retinal tracking software failures). Subjects were encouraged not to repeat trials
279 unless instructed to do so by the examiner. At each test location, at least three 20-trial
280 staircases were obtained.

281 After testing, the delivery location of each stimulus was identified by locating the digital
282 marker inserted into the video on the stimulus frames. For a trial to be included in subsequent
283 analyses, the delivery location for each stimulus frame had to fall within a 15-by-15 arcmin
284 inclusion window centered on the median delivery coordinates for all deliveries at that test
285 location. Psychometric functions were fit to the remaining data using the Palamedes toolbox²⁷;
286 threshold was defined as the test intensity that yielded 78% frequency-of-seeing. In cases
287 where 8 or more trials at the maximum deliverable stimulus intensity were not detected by the
288 subject, a sensitivity value of 0 dB was assigned (i.e. a *dense scotoma* at the modulation limits
289 of the system). For all other test locations, measurements where fewer than half of the total
290 trials (i.e., 30 out of 60, typically) were delivered accurately were excluded altogether. Threshold
291 intensities (I_t) were converted to sensitivity in decibels (S_{dB}) using the following formula: $S_{dB} = 10$
292 $* \log_{10}(I_{max}/I_t)$, where I_{max} represents the maximum stimulus intensity (~580 cd/m²; Weber
293 contrast = 42.9) the system is capable of presenting. For comparison, the Zeiss Humphrey Field
294 Analyzers HFA3 and the Nidek MP1 microperimeter have maximal stimulus luminances of
295 ~3000 cd/m² and ~125 cd/m², respectively.²⁸ The background on which the incremental stimuli
296 were presented was a combination of baseline light leak through the 550 nm AOM, the infrared
297 imaging light, and the dim wavefront sensing light; its cumulative luminance was approximately
298 13.5 cd/m², the majority of which was caused by the infrared imaging light. The dynamic range
299 of stimulus modulation was 24 dB; the dimmest non-zero stimulus corresponded to a Weber
300 contrast of 0.16.

301 Transverse chromatic aberration (TCA) causes a displacement between the imaging (848
302 nm) and stimulus (550 nm) beams at the retinal plane. Because AO microperimetry test
303 locations were selected in the coordinates of the infrared image used for retinal tracking, TCA
304 must be accounted for to enable a precise correlation of visual sensitivity to the underlying
305 mosaic structure. Before and after each measurement session, TCA was estimated using a
306 variant of a previously-published approach.²⁹ For each measurement, four 40-frame AOSLO
307 videos were acquired concurrently at the imaging and stimulus wavelengths. The spatial offsets
308 between corresponding infrared and visible-light video frames were estimated using full-frame

309 image registration.³⁰ The resultant shifts, in the x and y image dimensions, are a byproduct of
310 the laterally-displaced imaging and stimulation beams on the retina. TCA was defined as the
311 median x- and y-shift between each frame pair measured across the quartet of videos (160
312 samples total). The TCA shift information was used in offline analyses to refine the estimate of
313 stimulus delivery locations relative to the structures observed the infrared retinal images. Note
314 that imaging at the stimulus wavelength requires using light intensities that cause photopigment
315 bleaching. To allow the subjects to readapt, the eye selected for testing was patched for 10
316 minutes prior to beginning data collection.

317 In all 12 subjects, visual sensitivity was assessed at test locations spanning a lesion
318 boundary. To quantify the gradient of sensitivity near the atrophic border, the distance from
319 each test location to the nearest lesion border was estimated. This was done by placing a
320 measurement circle centered on each test location in the confocal image and expanding it
321 concentrically until the examiner judged that it encroached on the lesion; the distance to the
322 atrophic border was taken as the radius of this circle. We note that while the atrophic retina in
323 CHM is readily distinguishable from regions containing clear evidence of cone photoreceptors
324 (i.e. hexagonal packing), structural heterogeneity in the narrow transition zone makes it difficult
325 to apply an objective, image-based criterion for what constitutes the exact location of the
326 atrophic border in CHM.

327 In four subjects with whom we had additional time for testing, we also examined visual
328 sensitivity along ORTs protruding from the atrophic border. There were no systematic
329 differences between the subset selected for ORT testing and the larger cohort with respect to
330 age, central visual acuity, or extent of visual field (atrophic border locations can be inferred from
331 the test eccentricity column in **Table 1**).

332

333 **Results**

334 An example of the typical clinical assessment of retinal structure and function in a patient
335 with CHM is shown in **Figure 1**. Color fundus photography (**Figure 1A**) revealed a characteristic
336 posterior pole appearance, with a central island of preserved retina featuring scalloped edges.
337 In the circumjacent region, the retina and RPE were degenerated and deeper choroidal
338 structures and white sclera were visible. FAF imaging (**Figure 1B**) more clearly delineated these
339 features, with a central region of preserved FAF signal surrounded by hypo-FAF and
340 background autofluorescence areas. Microperimetry (Nidek MP1, 10-2 test pattern) sensitivity
341 values were generally well-correlated with the underlying, relatively preserved retina and RPE,
342 with some exceptions near the atrophic border (**Figure 1B**, red arrowheads). OCT imaging

343 **(Figure 1C)** showed relatively preserved retinal lamination in the intact retina, with an abrupt
344 transition in thickness occurring at the atrophic borders **(Figure 1C, white dashed lines)**. ORTs
345 were evident in regions with severely thinned but detectable outer nuclear layer (ONL overlaying
346 severely depigmented RPE, appearing in the OCT images as hyperreflective rings encircling
347 hyporefective cores **(Figure 1C, white arrowheads)**.

348 Multi-modal adaptive optics ophthalmoscopy demonstrated that contiguous mosaics of cone
349 photoreceptors were maintained up to the edge of the atrophic border. Example images from
350 two retinal eccentricities acquired from subject 13125 are shown in **Figure 2**. In the confocal
351 images (left column), the tightly-packed bright spots occupying the majority of the images
352 represent light reflected from individual cone photoreceptor outer segments. The co-localized
353 features observed in the split-detector images acquired simultaneously (right column) are
354 presumed to correspond to multiply-scattered light arising from the cone inner segment.¹⁸ In the
355 confocal images, the transition to the atrophic retina was often marked by a hyporefective band
356 in which cones appeared dim or not visible, followed by a hyperreflective region with a speckled
357 appearance. By contrast, split-detector imaging revealed more phenotypic heterogeneity in
358 outer retinal structure at the margin. In some cases, there appeared to be cones with a
359 disrupted orientation along the border, resembling felled trees **(Figure 2, top-right panel)**. The
360 furrowed appearance of the circumlesional region has been termed “variegated structure” by
361 previous investigators.³¹ Elsewhere, the transition from relatively normal inner segment mosaic
362 structure to the atrophic retina was more abrupt **(Figure 2, bottom-right panel)**.

363 AO microperimetry offers the stimulation resolution to probe cone-mediated function across
364 these cellular-scale phenotypic variations. Color-coded markers representing the measured
365 sensitivity of the underlying retina are shown in **Figure 2**. On this color scale, greenish markers
366 indicate areas where sensitivity was preserved, while red markers represent locations where the
367 subject was unable to detect the highest-intensity stimulus (i.e. scotomas). At both eccentricities
368 shown in **Figure 2**, sensitivity was maintained in regions where the cone mosaic structure was
369 relatively intact. As the atrophic border was approached, sensitivity dropped, and dense
370 scotomas were typically observed at and beyond the structural margin. Additional examples of
371 how sensitivity changes across the atrophic border in CHM are shown in **Figure 3**. Note that the
372 drop in sensitivity with change in test location is very rapid, and can occur across a retinal
373 region that is commensurate with the size of the Goldman III stimulus routinely used in clinical
374 microperimetry. Across all included trials, the precision of stimulus delivery (defined as the
375 standard deviation of the Euclidean distance from each delivery location to the center of the
376 inclusion window) was 1.25 arcmin, or approximately 6.1 μm .

377 Together, these results suggest that the gradient of sensitivity at the outer retinal transition
378 zone in CHM is steep. To examine this relationship more quantitatively, we plotted visual
379 sensitivity as a function of the distance to the atrophic border for each test point from our 12
380 subjects (**Figure 4**), excepting the measurements that were obtained across ORTs (see
381 **Figures 5** and **6**). One striking feature of these data was that essentially every test site located
382 within the atrophic retina (negative distances in **Figure 4**) exhibited a dense scotoma (i.e., 0 dB
383 sensitivity), including those situated directly adjacent to the atrophic border (red line). Moving
384 into the preserved retina, sensitivity recovered sharply with increasing distance from the lesion
385 margin, often improving by 10 dB (i.e. 1 log unit) or more across the distance subtended by the
386 Goldmann III stimulus used in clinical perimetry (gray shaded area, ~130 μm). It is worth noting
387 that we made no attempt in this summary analysis to account for inter-subject differences in test
388 eccentricity, stimulus size, or stage of degeneration, all of which impact visual sensitivity and
389 could introduce additional variability from subject to subject. Despite this, our aggregate results
390 demonstrate clearly that visual sensitivity falls precipitously at the atrophic border in CHM.

391 ORTs are a second phenotypic hallmark of outer retinal degenerations with prominent
392 associated RPE degeneration, including CHM. All 12 subjects in the present study exhibited
393 ORTs visible on OCT. Although histological³² and high-resolution retinal imaging^{16, 31} evidence
394 has accumulated to demonstrate that photoreceptor structure is partially preserved in ORTs, the
395 degree to which these remnant cones might support visual function is not clear. **Figure 5** shows
396 imaging and adaptive optics microperimetry data obtained along an ORT in subject 13195.
397 Consistent with other subjects with CHM, FAF imaging and MP1 sensitivities suggested a sharp
398 structural and functional transition at the atrophic border (**Figure 5A**). In the temporal retina,
399 OCT images (**Figure 5B**) revealed the cross-sectional structure at the atrophic border. In the
400 middle OCT image, the ELM appears to descend towards Bruch's membrane, suggesting the
401 scan passed through the longitudinal axis of an ORT protruding temporally. A split-detector
402 image obtained from this region confirmed the presence of an ORT in which remnant
403 photoreceptor inner segments appeared to be present (**Figure 5C**). AO microperimetry data
404 collected along the ORT demonstrated a steep decline in sensitivity with increasing distance
405 from the preserved retina, with dense scotomas (red markers) measured at the most distal loci.
406 A similar pattern of sensitivity along ORTs was observed in three additional subjects (**Figure 6**).

407

408 Discussion

409 The centripetal pattern of central photoreceptor loss in CHM implies that cones situated near
410 the atrophic border may be next to succumb to degeneration. Previous structural studies using

411 adaptive optics ophthalmoscopy have shown that contiguous cone mosaics are preserved close
412 to the atrophic border^{6, 15, 16, 31} but the degree to which these cones on the healthy side of the
413 border support visual function has been a critical and heretofore unanswered question. Using
414 adaptive optics microperimetry to assess visual function with cellular precision, we found a tight
415 relation between structure and function at the atrophic border in CHM: photopic visual sensitivity
416 was preserved in regions with a contiguous cone mosaic while dense scotomas were invariably
417 observed in atrophic areas (**Figure 4**). Unlike steep transitions in visual sensitivity documented
418 in conventional clinical microperimetry, AO microperimetry demonstrated a gradient of
419 sensitivity loss across the transition zones that co-localized with a progressively disorganized
420 cone mosaic. This finding suggests the structural disorganization of the cone photoreceptor
421 mosaic with photoreceptor loss and cone outer segment shortening and/or loss underlies the
422 cone sensitivity losses in CHM.

423 This finding not only has implications for our understanding of how CHM progresses
424 naturally, but also illustrates how adaptive optics microperimetry may fit into the complement of
425 tests used to evaluate the efficacy of novel treatments intended to slow down or reverse its
426 course. A number of clinical trials investigating gene therapies for CHM are currently ongoing,
427 with some promising early results.^{12, 13} The prospects for preserving or expanding the area of
428 visual function with these treatment approaches hinge on whether dysfunctional border cones
429 retain a capacity for driving downstream circuitry. Our finding of reduced-but-measurable
430 sensitivities within 30 arcmin (~150 μ m) of the atrophic retina suggests that improving function
431 at the margin of the intact retina with therapeutic interventions may indeed be possible. Further,
432 our finding of dense scotomas at and beyond the atrophic border suggests that structural
433 measurements, such as the width of intact outer retinal layers on OCT or the area of a
434 continuous photoreceptor mosaic on AO imaging, may be appropriate for use as outcome
435 measures for assessing therapeutic safety and efficacy. The fine-grained functional testing
436 offered by the AO microperimetry approach comes at the cost of limited retinal coverage and
437 high technical complexity, making it difficult to envision its translation into routine clinical use.
438 Nevertheless, our results highlight how clarifying structure-function relationships at the cellular
439 scale in a small experimental cohort may help validate the inferences made using ophthalmic
440 devices (e.g. OCT) better suited for large-scale studies.

441 The sensitivity with which any measurement can ascribe a gain (or loss) of function to a
442 treatment is critically limited by the measurement's test-retest variability. In the macula of CHM
443 patients, the repeatability of conventional microperimetry measurements obtained within the
444 preserved retina is roughly ± 5 dB.^{10, 33} However, near the atrophic border, test-retest variability

445 increases twofold, to ± 10 dB.¹⁰ This outcome could reflect genuine functional variability along
446 the atrophic border, or it could be due to limitations in the precision with which border regions
447 are stimulated. In normal subjects, test-retest variability is substantially higher for test points
448 near the optic nerve head compared to data obtained from the macular and peripapillary
449 regions,³⁴ suggesting that the poor repeatability stems in part from some stimuli inadvertently
450 landing in scotomatous locations. Likewise, in our own clinical microperimetry data in CHM, we
451 occasionally observed test loci within the atrophic zone that appeared to retain residual
452 sensitivity (**Figure 1**, red arrows). This could have been due to errant stimulus deliveries. The
453 cellular-scale delivery precision of adaptive optics microperimetry^{22, 24} helps resolve this
454 ambiguity: nearly every atrophic location we tested with this technique exhibited a dense
455 scotoma, even those positioned directly adjacent to contiguous cone mosaics (**Figure 4**).
456 Although practical considerations precluded us from conducting a formal analysis of test-retest
457 variability in the current study, our data suggest that the repeatability of adaptive optics
458 microperimetry measurements near degenerated retina will be less influenced by delivery
459 uncertainty, compared to data acquired with conventional perimetry devices.

460 Our results also provide new insights about the functional integrity of remnant cones located
461 within ORTs,³¹ a phenotypic signature encountered in many outer retinal degenerations with
462 potential RPE involvement, including CHM.^{8, 35} Evidence from histology^{32, 36} and longitudinal
463 OCT imaging³⁷ has led to a mechanistic model of ORT development in which RPE
464 degeneration in regions with photoreceptor degeneration triggers Müller glia cells to guide a
465 descent and eventual subduction of the ELM, ultimately forming a tubular structure containing
466 photoreceptors oriented radially towards the lumen. Abnormal cones with preserved inner and
467 outer segments, presumably in a nascent stage of degeneration, have been observed in ORTs
468 in histological preparations; as the degeneration progresses to end-stage, both inner and outer
469 segments are eventually lost.³²

470 Despite the findings demonstrating that the cellular morphology of cones situated in ORTs
471 can, in some cases, remain grossly intact, our measurements provided no evidence of visual
472 sensitivity for stimuli delivered along ORTs (**Figures 5 and 6**). While we cannot exclude the
473 possibility that larger or more intense stimuli may have evoked a residual response from these
474 cones, our results indicate that visual sensitivity within ORTs is, at minimum, severely
475 impoverished. This is perhaps not surprising, considering that the functional viability of these
476 photoreceptors would depend on additional factors, the most obvious being the existence of
477 healthy synaptic contacts with synaptic partners in the inner nuclear layer. Whether functional
478 synapses between affected cones and downstream bipolar cells are preserved after ORT

479 formation is not well-established. In addition, healthy cones act as optical waveguides, funneling
480 incident light into the outer segment for phototransduction. Similar to previous results,^{16, 31} we
481 found evidence of cone inner segments in ORTs using the split-detector modality (**Figures 5**
482 **and 6**). In the corresponding confocal images, however, cone mosaics were not well-resolved.
483 While this finding is consistent with the idea that the infolded architecture of ORTs disrupts
484 normal photoreceptor waveguiding,³⁸ we cannot exclude the possibility that adjustments to the
485 confocal imaging parameters (e.g. changes to the detection aperture size or imaging focal
486 depth) might reveal waveguiding cones not visible in the current images.³¹ Finally, normal
487 photoreceptors depend on the RPE for sustenance and regeneration of the visual pigment.
488 Longitudinal imaging studies have demonstrated that ORTs can remain stable over time,^{16, 31}
489 however, leading to the hypothesis that fluid exchange with nearby intact retina might provide
490 some replacement trophic support in the absence of underlying RPE.³⁶ It is not clear if this
491 nourishment would be sufficient to maintain an operational visual cycle. For example, previous
492 work suggests that cone photoreceptors exhibit delayed dark adaptation in choroideremia³⁹;
493 exposure to higher light levels (such as those used to measure TCA prior to testing) might
494 differentially affect the sensitivity of any remnant cones within the ORT.

495 The present results add to an emerging body of work in which adaptive optics has been
496 leveraged to examine, at the cellular scale, the relationship between structure and function in
497 retinal disease. In the first clinical application of high-resolution perimetry with adaptive optics,
498 Makous et al.⁴⁰ analyzed psychometric functions for detecting cone-sized stimuli delivered
499 without retinal tracking to infer the presence of microscotomas in a dichromatic patient whose
500 retina was missing roughly 30% of its cones. The incorporation of retinally-contingent stimulus
501 delivery methods into the AOSLO imaging modality²² has enabled more direct comparisons of
502 structure and function, including a few examples where the link between the two was
503 counterintuitive. In one patient with type 2 macular telangiectasia, cone-mediated sensitivity was
504 measured in locations where the confocal AO images suggested cone photoreceptors were
505 absent.⁴¹ Longitudinal AOSLO imaging in the same patient demonstrated how cone reflectivity
506 in the confocal modality can be capricious, with a contiguous mosaic of cones appearing in a
507 region near the temporal lesion border that previous images had suggested was devoid of
508 cones. More recently, further evidence for abnormally-reflecting cones with residual function
509 (termed “dysflective” cones) was reported in a patient with acute bilateral foveolitis.⁴² In the
510 current results, the link between cone mosaic structure and function was more straightforward,
511 with no evidence of preserved visual sensitivity in regions where cones were not resolved.
512 Collectively, however, these diverse findings underscore how incorporating functional testing at

513 a cellular scale helps refine and guide our interpretation of the ambiguous structures often
514 observed in high-resolution images of the diseased retina.

515 In summary, we used AO microperimetry to reveal a steep gradient in cone-mediated visual
516 sensitivity across the atrophic border in choroideremia. We also found precipitous drops in
517 sensitivity when stimuli were delivered along ORTs that appeared to contain cone inner
518 segments. In the future, cone-targeted microperimetry may be combined with other recently-
519 developed AOSLO techniques for probing photoreceptor function, including cellular-scale
520 measurements of rod sensitivity⁴³ and optophysiological assays of cone function,⁴⁴ to provide a
521 more complete assessment of outer retinal integrity in retinal dystrophy.

522

523 **Figure Captions:**

524

525 **Figure 1| Clinical assessment of structure and function in choroideremia.** (A) Color fundus
526 photograph from the left eye of subject 13125 showing a central island of preserved retina
527 bordered by scalloped edges demarcating the sharp transition to depigmentation of the RPE
528 and peripheral atrophy. (B) FAF image with 10-2 MP1 sensitivity values superimposed. The
529 region shown here is denoted by the black box in (A). The hyper-fluorescent region corresponds
530 to the autofluorescence signal and presumably delineates the boundaries of the viable retina.
531 The red circle indicates the subject's fovea. MP1 sensitivity values are shown numerically in
532 decibels (dB); a sensitivity value of 0 dB indicates a dense scotoma at that location on the
533 retina. Yellow arrowheads indicate locations where residual sensitivity appears to be preserved
534 near the atrophic border, whereas red arrows highlight locations in the atrophic retina with
535 reduced but still measurable sensitivity. Green scan lines indicate locations of the OCT B-scans
536 shown in (C). White boxes outline regions where AO microperimetry was conducted (see
537 **Figure 2**). (C) OCT B-scans corresponding to the lines in (B). Retinal lamination is mostly
538 preserved in regions co-localized with a measurable autofluorescence signature; the OCT layer
539 corresponding to the photoreceptor-RPE interdigitation zone is absent. Outer retinal structure
540 changes abruptly at the atrophic border (white dashed lines) with loss of the OCT layers
541 corresponding to the outer nuclear layer, the external limiting membrane, the ellipsoid zone (or
542 inner segment/outer segment junction) and the RPE. ORTs, visible as hyperreflective bands
543 encircling hyporefective cores, are indicated by white arrowheads. Scale bars in all panels
544 represent 3 degrees of visual angle.

545

546 **Figure 2| Cellular-scale retinal structure and function at the atrophic border measured**
547 **with AOSLO.** Spatially-registered confocal (left column) and split-detector (right column)
548 AOSLO images from the left eye of subject 13125. The top row images are centered roughly
549 1.25 degrees inferior-temporal from the fovea. The bottom row images were acquired 4.2
550 degrees from the fovea in the inferior retina. These retinal regions are outlined in white on the
551 FAF image in **Figure 1B**. Colored markers indicate the visual sensitivity at each AO
552 microperimetry test location. Markers are color-coded to reflect the measured sensitivity (in dB)
553 and scaled to represent the size of the microperimetry stimulus on the retina (upper row: 3.5
554 arcmin diameter; bottom row: 7.0 arcmin diameter). Stimulus markers were placed after
555 accounting for transverse chromatic aberration between the imaging and stimulus wavelengths.
556 The scale bar represents the retinal diameter of the Goldmann III perimetry stimulus (0.43
557 degrees) routinely used in clinical microperimetry.

558
559 **Figure 3| Additional examples of the sensitivity gradient at the atrophic border in CHM.**
560 As in Figure 2, the left column shows confocal images and the right column contains the
561 corresponding split-detector images. The test eccentricity, relative to the center of each image,
562 is indicated by the text to the left of each row. Sensitivity markers are scaled and color coded as
563 described in Figure 2. In the top and middle panels, the atrophic border runs across the upper
564 section of the image; in the bottom panels, the atrophic border is oriented vertically along the left
565 side of the image. In all three cases, visual sensitivity is maintained in areas with clearly-
566 resolved photoreceptors and drops off steeply as the atrophic border is approached. Dense
567 scotomas were measured at all test points located entirely within the severely degenerated
568 retina. Scale bars in all panels depict the size of the Goldmann III stimulus (0.43°).

569
570 **Figure 4| Visual sensitivity gradient at the atrophic border in CHM.** Visual sensitivity is
571 plotted as a function of distance to the lesion border (red line) for all subjects. Sensitivity is
572 shown in dB; the color scale used elsewhere in this report is included for reference. Points to
573 the left of the red line are located within the lesion. The gray shaded area represents the
574 diameter of the Goldmann III stimulus (0.43°).

575
576 **Figure 5| Reduced visual sensitivity along an ORT.** (A) MP1 10-2 microperimetry map
577 registered to the FAF image from the right eye of subject 13195. Green scan lines show the
578 location of the cross-sectional OCT images in (B) obtained near an ORT protruding from the

579 atrophic border in the temporal retina ($\sim 6^\circ$). The black box outlines the region shown at higher
580 resolution in (C). (B) OCT B-scans acquired along the atrophic border, the location of which is
581 indicated by the dashed white line. The middle OCT scan passes through the longitudinal axis
582 of the ORT. (C) Adaptive optics microperimetry visual sensitivity markers shown on the split-
583 detector AOSLO image. Sensitivity markers are scaled and color coded as described in Figure
584 3. Photoreceptor inner segments appear to be preserved well into the ORT, but sensitivity falls
585 off steeply with increasing distance from the base of the ORT. Scale bars in (A) and (B) are 3° ;
586 in (C), scale bar represents the Goldmann III stimulus (0.43°).

587

588 **Figure 6| Additional examples of dense scotomas along ORTs.** Adaptive optics
589 microperimetry results for test stimuli delivered along ORTs in three subjects. Cones and
590 variegated structures are observed in the split-detection AO images. In our apparatus, confocal
591 AO images do not show clearly waveguiding cones within the ORTs. All conventions as in
592 Figure 3.

593

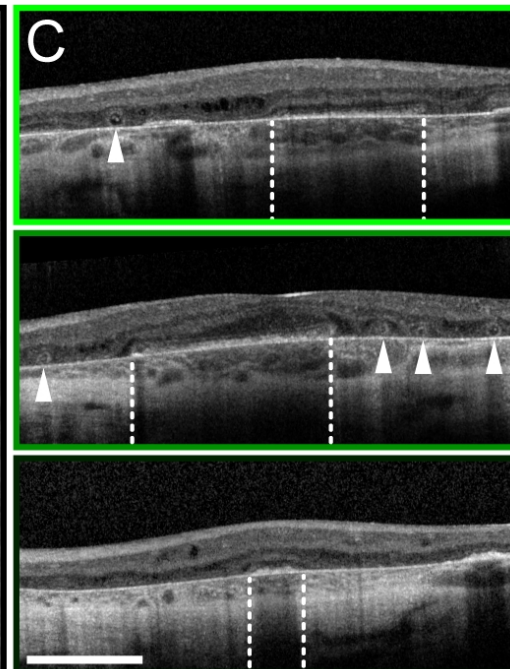
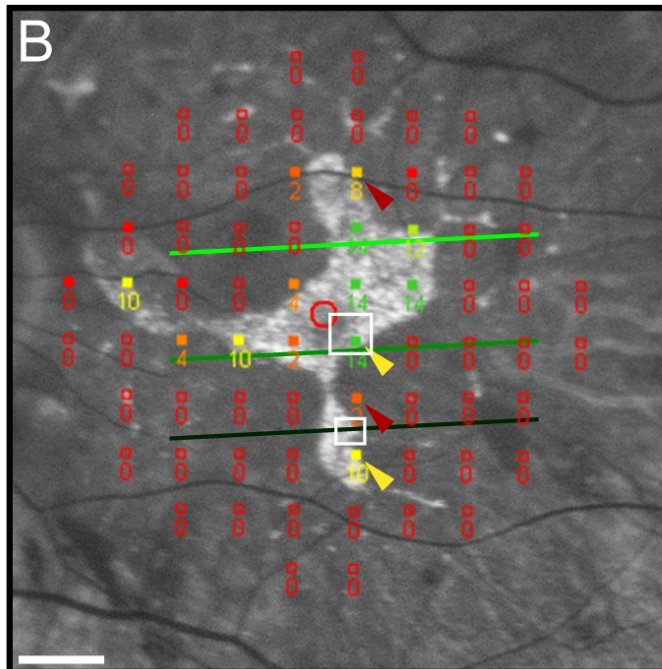
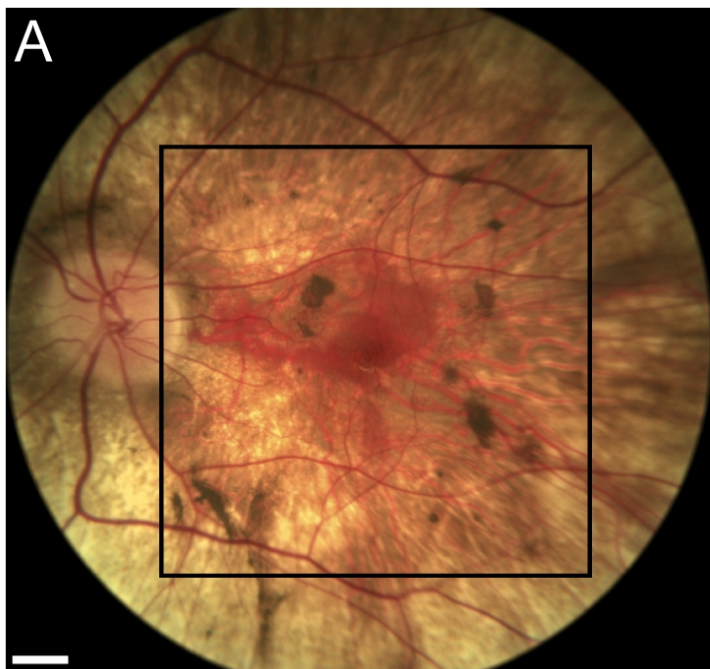
594 **References**

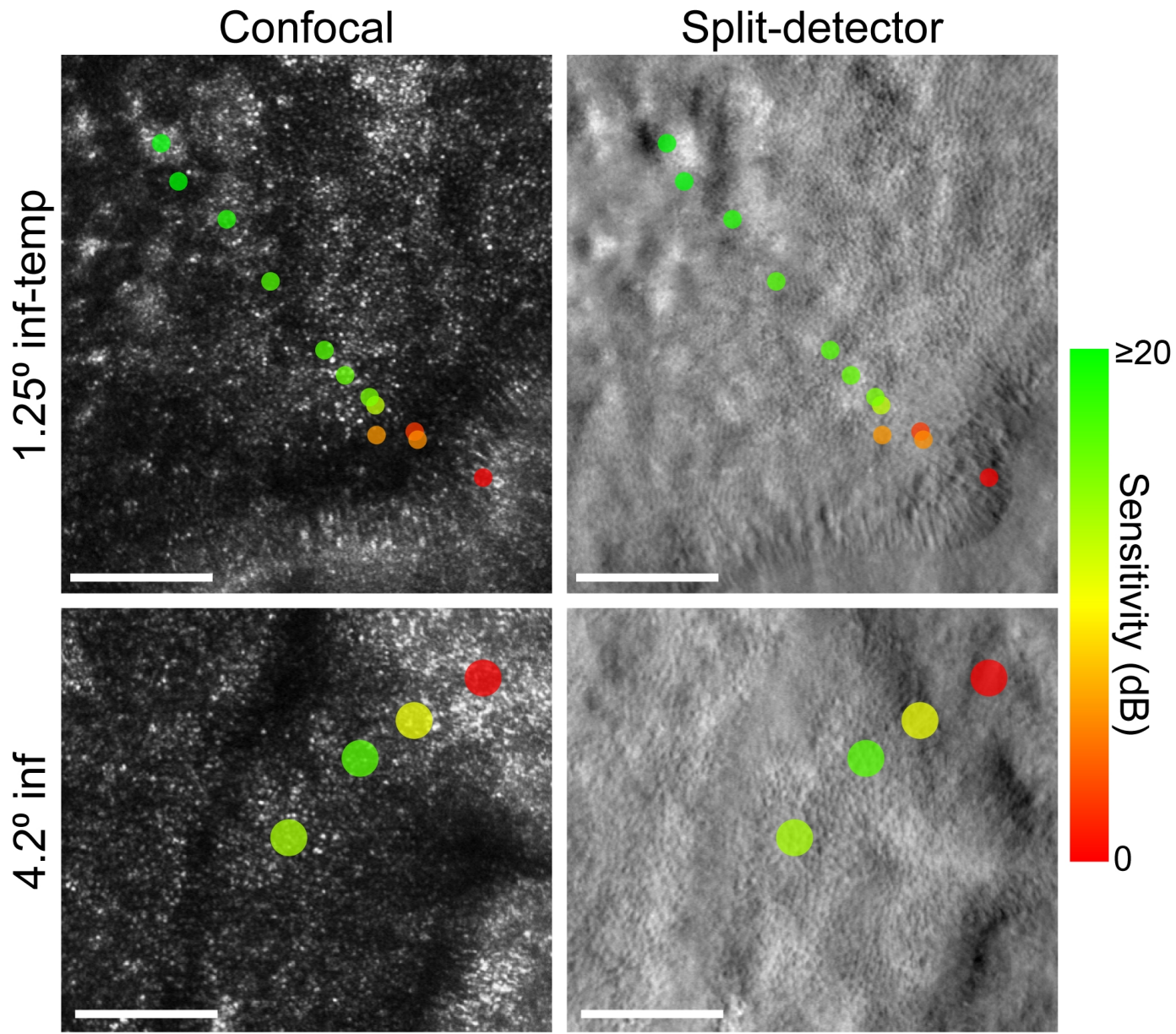
- 595 1. MacDonald I, Hume S, Chan S, et al. GeneReviews® [Internet]. In: Adam MP
596 AH, Pagon RA, et al., editors. , ed. Seattle (WA): University of Washington, Seattle,
597 2003 Feb 21 [Updated 2015 Feb 26]; v. 1993-2018. Available from:
598 <https://www.ncbi.nlm.nih.gov/books/NBK1337/>.
- 599 2. McTaggart KE, Tran M, Mah DY, et al. Mutational analysis of patients with the
600 diagnosis of choroideremia. *Human mutation* 2002;20(3):189-96.
- 601 3. Preising M, Ayuso C. Rab escort protein 1 (REP1) in intracellular traffic: a
602 functional and pathophysiological overview. *Ophthalmic genetics* 2004;25(2):101-10.
- 603 4. Aleman TS, Han G, Serrano LW, et al. Natural History of the Central Structural
604 Abnormalities in Choroideremia: A Prospective Cross-Sectional Study. *Ophthalmology*
605 2017;124(3):359-73.
- 606 5. Coussa RG, Traboulsi EI. Choroideremia: a review of general findings and
607 pathogenesis. *Ophthalmic genetics* 2012;33(2):57-65.
- 608 6. Morgan JI, Han G, Klinman E, et al. High-resolution adaptive optics retinal
609 imaging of cellular structure in choroideremia. *Investigative ophthalmology & visual*
610 *science* 2014;55(10):6381-97.

- 611 7. Jacobson SG, Cideciyan AV, Sumaroka A, et al. Remodeling of the human retina
612 in choroideremia: rab escort protein 1 (REP-1) mutations. *Investigative ophthalmology &*
613 *visual science* 2006;47(9):4113-20.
- 614 8. Heon E, Alabduljalil T, McGuigan ID, et al. Visual Function and Central Retinal
615 Structure in Choroideremia. *Investigative ophthalmology & visual science*
616 2016;57(9):OCT377-87.
- 617 9. Coussa RG, Kim J, Traboulsi EI. Choroideremia: effect of age on visual acuity in
618 patients and female carriers. *Ophthalmic genetics* 2012;33(2):66-73.
- 619 10. Dimopoulos IS, Tseng C, MacDonald IM. Microperimetry as an Outcome
620 Measure in Choroideremia Trials: Reproducibility and Beyond. *Investigative*
621 *ophthalmology & visual science* 2016;57(10):4151-61.
- 622 11. Dimopoulos IS, Freund PR, Knowles JA, MacDonald IM. The Natural History of
623 Full-Field Stimulus Threshold Decline in Choroideremia. *Retina* 2018;38(9):1731-42.
- 624 12. MacLaren REG, M., Barnard, A.R., Cottrill, C.L., Tolmachova, T., Seymour, L.,
625 Clark, K.R., During, M.J., Cremers, F.P.M., Black, G.C.M., Lotery, A.J., Downes, S.M.,
626 Webster, A.R., Seabra, M.C. Retinal gene therapy in patients with choroideremia: initial
627 findings from a phase 1/2 clinical trial. *The Lancet* 2014.
- 628 13. Edwards TL, Jolly JK, Groppe M, et al. Visual Acuity after Retinal Gene Therapy
629 for Choroideremia. *The New England journal of medicine* 2016;374(20):1996-8.
- 630 14. Roorda A, Romero-Borja F, Donnelly III WJ, et al. Adaptive optics scanning laser
631 ophthalmoscopy. *Optics Express* 2002;10(9):405-12.
- 632 15. Syed R, Sundquist SM, Ratnam K, et al. High-resolution images of retinal
633 structure in patients with choroideremia. *Investigative ophthalmology & visual science*
634 2013;54(2):950-61.
- 635 16. Sun LW, Johnson RD, Williams V, et al. Multimodal Imaging of Photoreceptor
636 Structure in Choroideremia. *PLoS one* 2016;11(12):e0167526.
- 637 17. Dubra A, Sulai Y. Reflective afocal broadband adaptive optics scanning
638 ophthalmoscope. *Biomedical optics express* 2011;2(6):1757-68.
- 639 18. Scoles D, Sulai YN, Langlo CS, et al. In vivo imaging of human cone
640 photoreceptor inner segments. *Investigative ophthalmology & visual science*
641 2014;55(7):4244-51.
- 642 19. Atchison DA, Smith G. Chromatic dispersions of the ocular media of human
643 eyes. *Journal of the Optical Society of America A, Optics, image science, and vision*
644 2005;22(1):29-37.

- 645 20. Bennett AG, Rudnicka AR, Edgar DF. Improvements on Littmann's method of
646 determining the size of retinal features by fundus photography. Graefe's archive for
647 clinical and experimental ophthalmology = Albrecht von Graefes Archiv fur klinische und
648 experimentelle Ophthalmologie 1994;232(6):361-7.
- 649 21. Dubra A, Harvey Z. Registration of 2D Images from Fast Scanning Ophthalmic
650 Instruments. Lecture Notes in Computer Science 2010;6204:60-71.
- 651 22. Tuten WS, Tiruveedhula P, Roorda A. Adaptive optics scanning laser
652 ophthalmoscope-based microperimetry. Optometry and vision science : official
653 publication of the American Academy of Optometry 2012;89(5):563-74.
- 654 23. Tuten WS, Cooper RF, Tiruveedhula P, et al. Spatial summation in the human
655 fovea: Do normal optical aberrations and fixational eye movements have an effect?
656 Journal of vision 2018;18(8):6.
- 657 24. Arathorn DW, Yang Q, Vogel CR, et al. Retinally stabilized cone-targeted
658 stimulus delivery. Optics express 2007;15(21):13731-44.
- 659 25. Yang Q, Arathorn DW, Tiruveedhula P, et al. Design of an integrated hardware
660 interface for AOSLO image capture and cone-targeted stimulus delivery. Optics express
661 2010;18(17):17841-58.
- 662 26. King-Smith PE, Grigsby SS, Vingrys AJ, et al. Efficient and unbiased
663 modifications of the QUEST threshold method: theory, simulations, experimental
664 evaluation and practical implementation. Vision research 1994;34(7):885-912.
- 665 27. Prins N, Kingdom FAA. Applying the Model-Comparison Approach to Test
666 Specific Research Hypotheses in Psychophysical Research Using the Palamedes
667 Toolbox. Frontiers in psychology 2018;9:1250.
- 668 28. Acton JH, Bartlett NS, Greenstein VC. Comparing the Nidek MP-1 and
669 Humphrey field analyzer in normal subjects. Optometry and vision science : official
670 publication of the American Academy of Optometry 2011;88(11):1288-97.
- 671 29. Harmening WM, Tiruveedhula P, Roorda A, Sincich LC. Measurement and
672 correction of transverse chromatic offsets for multi-wavelength retinal microscopy in the
673 living eye. Biomedical optics express 2012;3(9):2066-77.
- 674 30. Guizar-Sicairos M, Thurman ST, Fienup JR. Efficient subpixel image registration
675 algorithms. Optics letters 2008;33(2):156-8.
- 676 31. King BJ, Sapoznik KA, Elsner AE, et al. SD-OCT and Adaptive Optics Imaging of
677 Outer Retinal Tubulation. Optometry and vision science : official publication of the
678 American Academy of Optometry 2017;94(3):411-22.

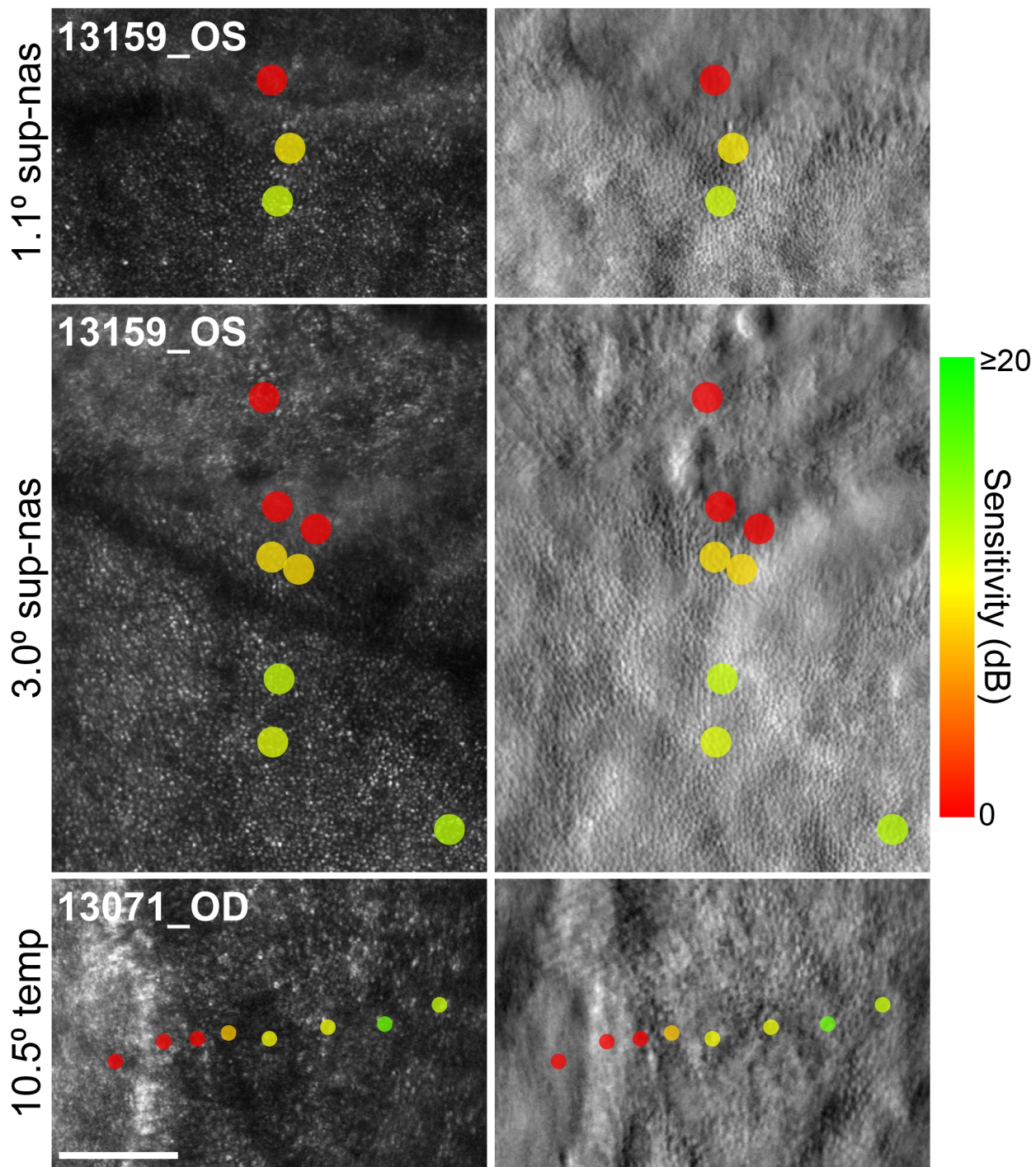
- 679 32. Schaal KB, Freund KB, Litts KM, et al. OUTER RETINAL TUBULATION IN
680 ADVANCED AGE-RELATED MACULAR DEGENERATION: Optical Coherence
681 Tomographic Findings Correspond to Histology. *Retina* 2015;35(7):1339-50.
- 682 33. Jolly JK, Xue K, Edwards TL, et al. Characterizing the Natural History of Visual
683 Function in Choroideremia Using Microperimetry and Multimodal Retinal Imaging.
684 *Investigative ophthalmology & visual science* 2017;58(12):5575-83.
- 685 34. Wu Z, Jung CJ, Ayton LN, et al. Test-Retest Repeatability of Microperimetry at
686 the Border of Deep Scotomas. *Investigative ophthalmology & visual science*
687 2015;56(4):2606-11.
- 688 35. Goldberg NR, Greenberg JP, Laud K, et al. Outer Retinal Tubulation in
689 Degenerative Retinal Disorders. *Retina* 2013.
- 690 36. Litts KM, Messinger JD, Dellatorre K, et al. Clinicopathological correlation of
691 outer retinal tubulation in age-related macular degeneration. *JAMA ophthalmology*
692 2015;133(5):609-12.
- 693 37. Dolz-Marco R, Litts KM, Tan ACS, et al. The Evolution of Outer Retinal
694 Tubulation, a Neurodegeneration and Gliosis Prominent in Macular Diseases.
695 *Ophthalmology* 2017;124(9):1353-67.
- 696 38. Litts KM, Wang X, Clark ME, et al. Exploring Photoreceptor Reflectivity through
697 Multimodal Imaging of Outer Retinal Tubulation in Advanced Age-Related Macular
698 Degeneration. *Retina* 2017;37(5):978-88.
- 699 39. Mura M, Sereda C, Jablonski MM, et al. Clinical and functional findings in
700 Choroideremia due to complete deletion of the *CHM* gene. *Arch Ophthalmol.* 2007;
701 125(8):1107-1113.
- 702 40. Makous W, Carroll J, Wolfing JI, et al. Retinal microscotomas revealed with
703 adaptive-optics microflashes. *Investigative Ophthalmology & Visual Science*
704 2006;47(9):4160-7.
- 705 41. Wang Q, Tuten WS, Lujan BJ, et al. Adaptive optics microperimetry and OCT
706 images show preserved function and recovery of cone visibility in macular telangiectasia
707 type 2 retinal lesions. *Investigative ophthalmology & visual science* 2015;56(2):778-86.
- 708 42. Tu JH, Foote KG, Lujan BJ, et al. Dysflective cones: Visual function and cone
709 reflectivity in long-term follow-up of acute bilateral foveolitis. *American journal of*
710 *ophthalmology case reports* 2017;7:14-9.
- 711 43. Domdei N, Domdei L, Reiniger JL, et al. Ultra-high contrast retinal display system
712 for single photoreceptor psychophysics. *Biomedical optics express* 2018;9(1):157-72.
- 713 44. Cooper RF, Tuten WS, Dubra A, et al. Non-invasive assessment of human cone
714 photoreceptor function. *Biomedical optics express* 2017;8(11):5098-112.

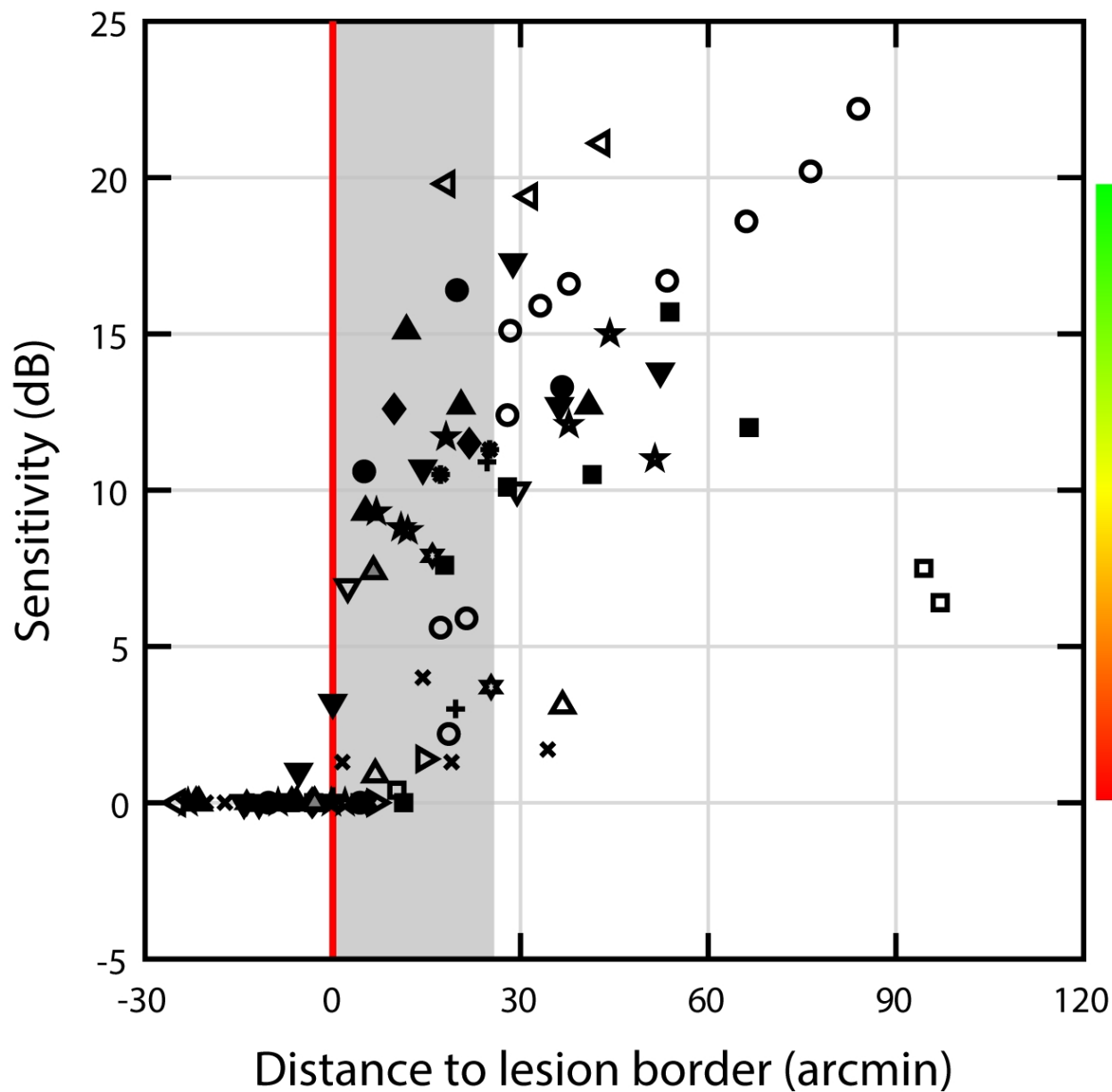




Confocal

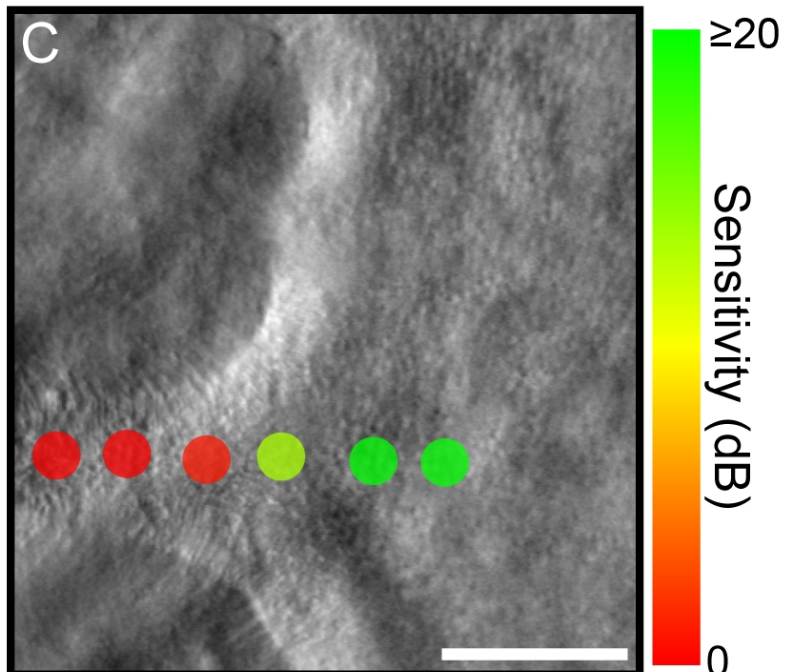
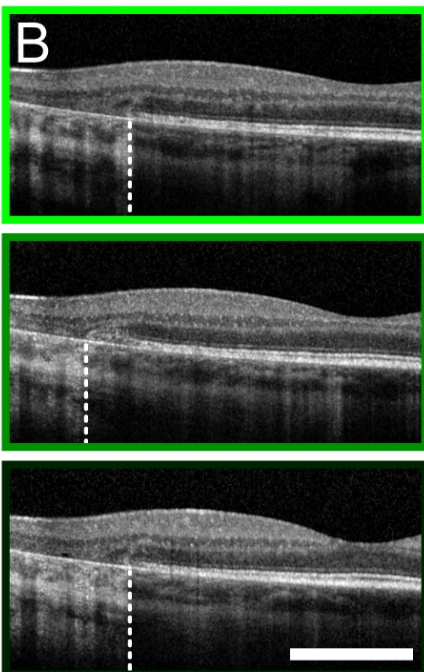
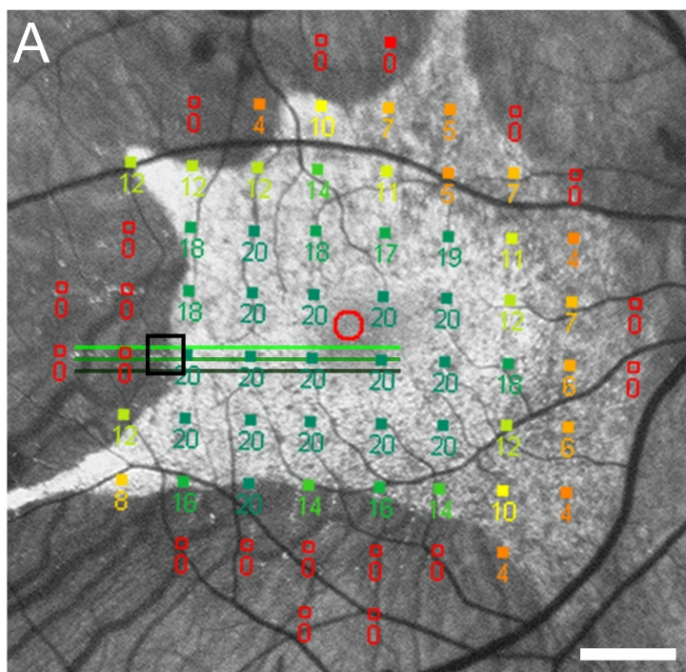
Split-detector





Legend:

- ✱ 13004, Visit 1, 4 N
- ✕ 13035, Visit 1, 2 N
- +
 13048, Visit 1, 6.2 T
- ◆ 13057, Visit 1, 2.8 S-T
- 13071, Visit 1, 10.5 T
- 13071, +6 mos., 10.5 T
- 13125, Visit 1, 1.25 I-T
- 13125, Visit 1, 4.2 I
- ☆ 13131, Visit 1, 4 S-N
- △ 13131, +6 mos., 0.8 T
- ★ 13159, Visit 1, 3 N
- ★ 13159, Visit 1, 1.1 S-N
- ▼ 13195, Visit 1, 6 T
- △ 13224, Visit 1, 8 T
- ▲ 13224, +6 mos., 8 T
- ▲ 13224, +12 mos., 8 T
- ▽ 13226, Visit 1, 3.8 T
- ▷ 13249, Visit 1, 5 N



Confocal

Split-detector

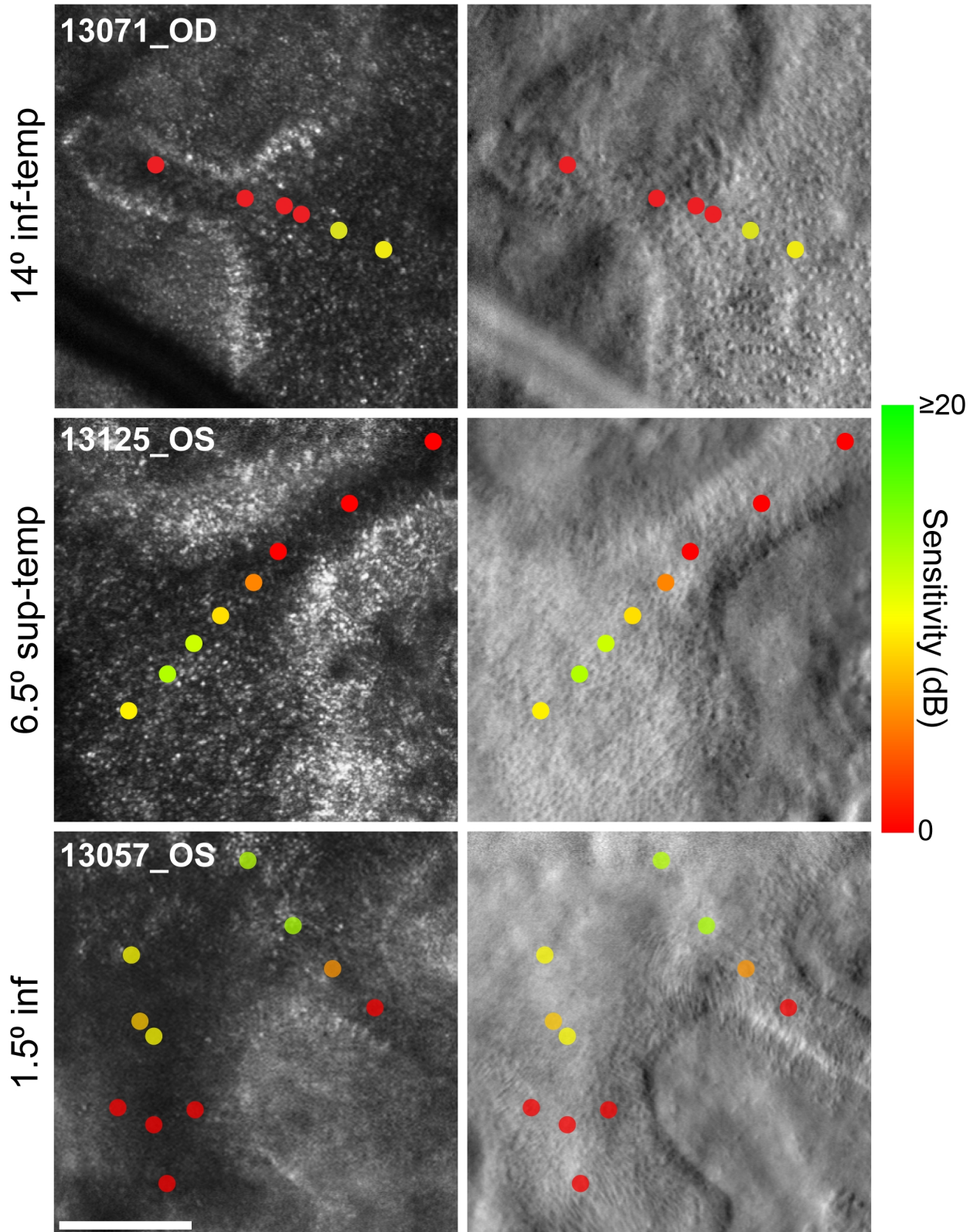


Table 1| Subject information

Patient ID	Genetic Mutation	Age	Eye Tested	Axial Length (mm)	Visual Acuity	Test Eccentricity* (°)	Stimulus Diameter (arcmin)	Visit†
13004	CHM Deletion, Exon 1-hemizygous-EPP=3	53	OS	26.86	20/20-2	4 N	3.5	Visit 1
13035	CHM Hemizygous c.315_318delTCAG	21	OD	24.51	20/32-4	2 N	7.0	Visit 1
13048	CHM Hemizygous c.700A>T/ p.Lys234Term	27	OD	24.39	20/20-2	6.2 T	7.0	Visit 1
13057	CHM Hemizygous for the Novel c.745delT mutation	36	OS	27.04 26.85	20/40 20/32-3	2.8 S-T 1.5 I	3.5 3.5	Visit 1 +5 mos.
13071	CHM- Glu382Stop GAA>TAA hemizygous-Epp=3	35	OD	23.88 23.91 23.91	20/25 20/25-4 20/20-4	10.5 T 10.5 T 14 I-T	3.5 3.5 7.0	Visit 1 +6 mos. +12 mos.
13125	CHM Hemizygous c.1437dupA/ p.Glu480ArgfsX12	34	OS	23.42 23.47	20/20-2 20/25-4	1.25 I-T 4.2 I 6.5 S-T	3.5 7.0 3.5	Visit 1 Visit 1 +6 mos.
13131	CHM-Met443 del2aacAT hemizygous-EPP=3	39	OD	24.99 24.97 24.97	20/20-2 20/25 20/25	4 S-N 4 S-N 0.8 T	3.5 7.0 7.0	Visit 1 +6 mos. +6 mos.
13159	CHM-Glu382Stop GAA>TAA hemizygous-EPP=3	45	OS	25.25 25.25	20/25 20/25	3 N 1.1 S-N	7.0 7.0	Visit 1 Visit 1
13195	CHM-IVS6-2 A>G hemizygous-EPP=3	38	OD	23.44	20/20	6 T	7.0	Visit 1
13224	CHM-Hemizygous c.41dupT/p.Gly15ArgfsX6	58	OS	24.30 24.27 24.31	20/20 20/20 20/20	8 T 8 T 8 T	7.0 7.0 7.0	Visit 1 +6 mos. +12 mos.
13226	CHM-IVS7-2 A>T hemizygous-EPP=3	41	OS	23.87	20/20-1	3.8 T	3.5	Visit 1
13249	CHM-Phe282 del2gtcTT hemizygous - EPP=3	20	OS	24.14	20/20	5 N	3.5	Visit 1

*eccentricity relative to fovea; S = superior; I = inferior; N = nasal; T = temporal

†relative to Visit 1